

An enhanced fault-detection method based on adaptive spectral decomposition and super-resolution deep learning

Zhenyu Yuan¹, Handong Huang¹, Yuxin Jiang², Jinbiao Tang², and Jingjing Li³

Abstract

Coherence is widely used for detecting faults in reservoir characterization. However, faults detected from coherence may be contaminated by some other discontinuities (e.g., noise and stratigraphic features) that are unrelated to faults. To further improve the accuracy and efficiency of coherence, preprocessing or postprocessing techniques are required. We developed an enhanced fault-detection method with adaptive scale highlighting and high resolution, by combining adaptive spectral decomposition and super-resolution (SR) deep learning into coherence calculation. As a preprocessing technique, adaptive spectral decomposition is first proposed and applied on seismic data to get a dominant-frequency-optimized amplitude spectrum, which has features of scale focus and multiple resolution. Eigenstructure-based coherence with dip correction is then calculated to delineate fault discontinuities. Following the remarkable success of SR deep learning in image reconstruction, a convolutional neural network (CNN) model is built and it then takes fault-detection images as the input to achieve enhanced results. The effectiveness of our proposed method is validated on a seismic survey acquired from Eastern China. Examples demonstrate that coherence from adaptive amplitude spectrum without dip correction is comparable to the dip-corrected one from seismic amplitude data at a certain degree, and they even highlight the specific scale of fault targets. Comparing fault detections from adaptive spectrum and some specific-frequency components, it can be concluded that adaptive spectral-based coherence highlights the primary scale of faults at various depths with only one single volume of data, thus improving the interpretation efficiency and reducing storage cost. Furthermore, with the trained CNN model, the resolution and signal-to-noise ratio of coherence images are effectively improved and the continuity of detected fault is promisingly enhanced.

Introduction

The geometry of faults and fracture network plays an important role in hydrocarbon accumulation and migration; hence, its identification is necessary and worthwhile. Integrating the information of adjacent seismic traces and samples in a nonlinear manner to measure waveform changes and delineate discontinuities directly, coherence (Bahorich and Farmer, 1995; Marfurt et al., 1998; Gersztenkorn and Marfurt, 1999; Gersztenkorn et al., 1999; Marfurt et al., 1999; Chopra et al., 2000; Bakker, 2002; Chopra, 2002; Hale, 2009; Wu, 2017) plays an important role in enabling interpreters to quickly visualize and map complex fault systems. With improved lateral resolution, eigenstructure-based coherence (Gersztenkorn and Marfurt, 1999) is widely used in fault detection.

It is known that seismic attributes are sensitive to the quality of the seismic data used. Low-quality data with strong noise and low resolution are difficult to use to extract valid geologic features. In addition, because

of thickness tuning effects, spectral components of specific frequency may highlight a certain scale of features than other specific-frequency components or broadband seismic reflections. Based on pure coherence, some enhanced processes, such as spectral decomposition (Wang et al., 2002) and image processing (AlBin-Hassan and Marfurt, 2003) were introduced to improve the performance of fault detection.

Considering that seismic response of a given geologic structure varies at different spectral bands, spectral decomposition is often used as a type of interpretation tool to highlight geologic target of a certain scale. For fault detection, combination of spectral decomposition and coherence is usually used to enhance illumination of certain scale of faults (Wang et al., 2002, 2016; Alaei, 2012; Chopra and Marfurt, 2016; Alaei and Torabi, 2017). The combination works well, but to get a more detailed view, interpreters need to generate tens of spectral components with a high storage requirement and cumbersome manual comparison. Sometimes, red-green-blue (RGB)

¹China University of Petroleum-Beijing, Beijing, China. E-mail: zhenyuyuan@outlook.com; webhhd@163.com.

²PST Service Corporation, Beijing, China. E-mail: jiangyuxin@pst-oil.com; tjb@ldocean.com.cn.

³Beijing Power Concord Technology Co. Ltd., Beijing, China. Email: jjenny.li@outlook.com.

Manuscript received by the Editor 30 September 2018; revised manuscript received 28 April 2019. ; published online 7 August 2019. This paper appears in *Interpretation*, Vol. 7, No. 3 (August 2019); p. T713–T725, 15 FIGS.

<http://dx.doi.org/10.1190/INT-2018-0180.1>. © 2019 Society of Exploration Geophysicists and American Association of Petroleum Geologists. All rights reserved.

or RGB α color blending techniques are used to integrate multiple components (Li and Lu, 2014; Honório et al., 2017). However, color blending is limited to handle only three or four of them. To address these limitations, Marfurt (2017) and Li et al. (2018) develop a multispectral coherence algorithm by incorporating multiple spectral components into a covariance matrix (Sui et al., 2015). Multispectral coherence shows the advantages of a higher signal-to-noise ratio (S/N) and resolution, as well as the enhanced ability of delineating complex architectures.

However, when integrating multiple spectral components to get a single coherence volume, it is possible to undergo risks of overprinting as in broadband coherence, depending on the number of spectral components. From another perspective, the spectral component at dominant frequency can highlight the geologic target of primary scale, and one spectrum volume adaptively extracted at varying dominant frequencies along depth exhibits multiscale feature. Following Yuan et al. (2015), adaptive spectral decomposition could be introduced as a preprocessing step of coherence calculation to highlight primary scale of geologic discontinuity at varying depths. The above combination can accelerate fault interpretation and reduce time and memory consumption.

Besides the combination of spectral analysis, image processing technologies are often introduced into coherence calculation to enhance the performance of fault detection. Historically, many filters, including multistage median-based modified trimmed-mean filter (Wu and Kundu, 1991), structure-oriented smoothing with edge-preserving (Höcker and Fehmers, 2002; Luo et al., 2002; Fehmers and Höcker, 2003; Wu and Guo, 2019), principal-component filter (Marfurt, 2006), are used to reduce noise, preserve edges, and preserve subtle lineaments in seismic interpretation (Al-Dossary and Marfurt, 2007). However, with the above filters, less effort has been directed toward fault enhancement and analysis (Machado et al., 2016). Recently, based on eigenvector analysis of discontinuities (Barnes, 2006), Machado et al. (2016) propose a directional Laplacian of a Gaussian (LoG) operator, which better characterizes orientation during discontinuity sharpening. Combined with structure-oriented filter as a preprocessing step, the LoG operator is introduced into coherence calculation for enhanced fault mapping (Chopra and Marfurt, 2017; Qi et al., 2017). Some other processing techniques, including ant tracking (Pedersen et al., 2002, 2003), fault-oriented scanning (Cohen et al., 2006; Hale, 2013; Wu and Hale, 2016; Wu and Zhu, 2017), and optimal surface voting (Wu and Fomel, 2018), are also used to enhance fault features while suppressing noisy features (unrelated to faults) in a seismic attribute image.

Other than those physics-driven filters, some data-driven methods could take effect with the availability of big data as well as development of efficient computing hardware and deep-learning algorithms. As a commonly used filter in image processing, convolution

filtering can be directly incorporated into fault detection to perform edge detection or to sharpen geometric attributes and then get enhanced fault images. Furthermore, the convolution filter is commonly used in image processing for feature extraction and is also the core block of convolutional neural networks (CNNs) (LeCun et al., 1990). CNNs have achieved many practical successes and were widely adopted in computer vision community, making itself a successful and dominant deep learning architecture (LeCun et al., 2015). Recently, the CNNs have been introduced to seismic interpretation for detecting faults (Huang et al., 2017; Di et al., 2018; Guo et al., 2018a; Wu et al., 2018, 2019; Zhao and Mukhopadhyay, 2018), channels (Pham et al., 2018), and salt bodies (Shi et al., 2018). In this paper, we use a CNN to improve the resolution and continuity of the faults features of a computed coherence image. Optimizing an end-to-end mapping between the low-resolution (LR) and high-resolution (HR) images, a deep CNN (called SRCNN) was successfully constructed to perform single-image super-resolution (SR) (Dong et al., 2016). SRCNN integrated multiple stages of SR reconstruction into a CNN model (the so-called end-to-end) and has achieved state-of-the-art performance. Benefiting from the strong capacity of extracting effective high-level abstractions, which bridge the LR and HR spaces, more effective CNN-based SR architectures were presented and have achieved significant improvements, quantitatively and qualitatively (Yang et al., 2018). Considering the success of SR deep learning in image processing, it can be incorporated into fault detection to improve the resolution and interpretability of coherence images.

Inspired by the scale focus and multiple resolution features of adaptive spectral decomposition and image enhancement of SR deep learning, we propose an enhanced fault-detection method. The new proposed method integrates adaptive spectral decomposition technique, SR deep-learning algorithm, and coherence calculation. The rest of the paper is arranged as follows. We first present an integrated workflow and introduce the relevant theoretical methods. Then, to demonstrate the performance and advantage of the proposed method, some examples are exhibited and analyzed. Finally, we draw some conclusions.

Methods

The implementation of our new enhanced fault-detection method consists of some essential techniques, such as adaptive spectral decomposition, coherence calculation, and SR deep learning and processing. The workflow is as follows (Figure 1):

- Perform spectral decomposition of a 3D seismic data by the generalized S transform and get dominant-frequency-optimized 3D amplitude spectrum from 4D time-frequency spectral data adaptively.
- Taking the amplitude spectrum at the dominant frequency as input, the coherence cube is calcu-

lated by using an eigenstructure-based coherence algorithm with dip correction.

- Perform fault-detection enhancement with the SR image-processing technique, in which certain CNN models should be first prepared by deep learning on appropriate data sets.

Then, we introduce the theories and implementations of the three mentioned methods in detail.

Adaptive spectral decomposition

The generalized S transform (Pinnegar and Mansinha, 2003) is used here to perform spectral decomposition:

$$S(\tau, f, \sigma) = \int_{-\infty}^{\infty} h(t) w(\tau - t, f, \sigma) e^{-i2\pi f t} dt, \quad (1)$$

where $h(t)$ and $S(\tau, f, \sigma)$ are the original time-domain signal and transformed time-frequency signal and $w(\tau, f, \sigma)$ indicates the generalized Gaussian window, with an additional parameter σ relative to the original S transform (Stockwell et al., 1996):

$$w(\tau, f, \sigma) = \frac{|f|}{\sqrt{2\pi}\sigma} e^{-\frac{f^2 \tau^2}{2\sigma^2}}, \quad \sigma > 0. \quad (2)$$

The generalized S transform permits the use of windows having frequency dependence in their shape in addition to width and height. It provides more adaptive multiresolution analysis, and it retains the property of invertibility of the original S transform and its relation to Fourier transform.

After spectral decomposing of 3D seismic data, 4D spectrum data with an additional frequency dimension are acquired. By computing the dominant frequency at each time sample and extracting the corresponding amplitude spectrum value, we finally achieve a 3D dominant-frequency amplitude spectrum volume. We call this process to acquire the dominant-frequency amplitude spectrum is called adaptive spectral decomposition.

Due to wave-propagation attenuation, the dominant frequencies of seismic data usually decrease with depth (Guo et al., 2018b, 2018c). In Figure 2, the dominant-frequency amplitude spectrum (Figure 2c) of certain inline section and its corresponding frequency profile (Figure 2b) are displayed. The frequency profile shows an obvious frequency decrease with depth (or time). To illustrate the advantage of adaptive spectral decomposition, specific-frequency amplitude spectra at 10, 30, and 60 Hz (Figure 2d–2f) are presented with the same value range of the dominant-frequency amplitude spec-

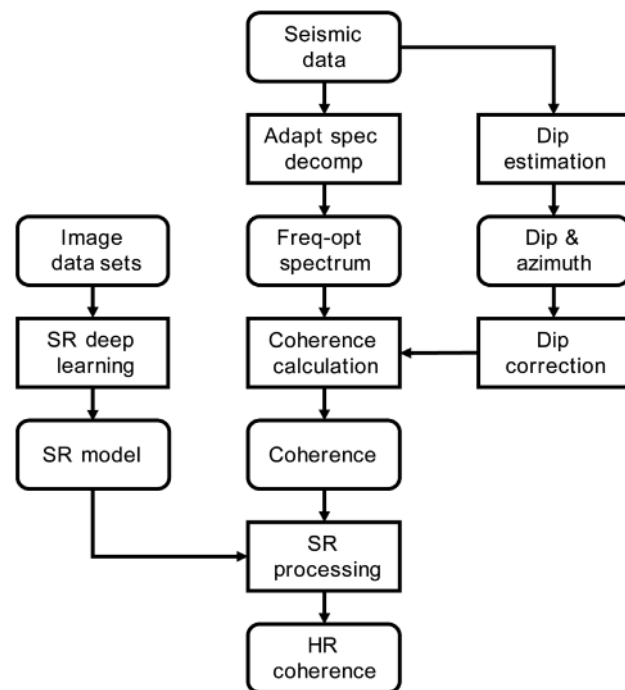


Figure 1. Workflow of the proposed enhanced fault-detection method, where the rounded rectangle and the rectangle indicate data and processing, respectively, and adapt spec decomp, freq-opt spectrum, SR, and HR are abbreviations of adaptive spectral decomposition, dominant-frequency-optimized amplitude spectrum, super-resolution, and high-resolution in sequence. The workflow includes three stages: adaptive spectral decomposition, spectral-based coherence calculation, and SR deep-learning fault enhancement.

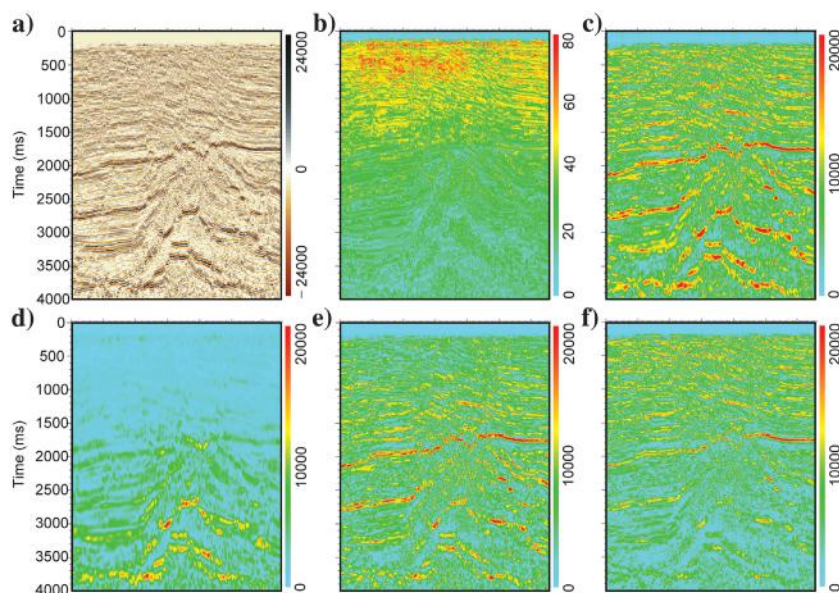


Figure 2. Adaptive spectral decomposition performance illustrated with a seismic section: (a) seismic amplitude, (b) dominant frequency with unit Hz, (c) frequency-optimized amplitude spectrum, and (d–f) corresponds to an amplitude spectrum of 10, 30, and 60 Hz.

trum to make some comparisons. The reason why frequency 10, 30, and 60 Hz are chosen is because they represent low, medium, and high frequency, respectively, inferring from the statistic spectrum of input seismic data (Figure 3). Corresponding to the dominant frequency distribution, seismic energy focuses from shallow to deep strata with decreasing frequency (from Figure 2d to Figure 2f). It is obvious that specific-frequency spectra mainly highlight geologic structures of specific scales. In another word, for certain scale of geologic target, only spectral component of specific frequency band works well. In contrast, dominant-frequency spectrum presents primary scale of structures at various depth (or time), displaying multiscale focusing ability. This principle provides guidance for later coherence calculation to highlight primary scale of faults with only one dominant-frequency-optimized spectrum data.

Coherence based on eigenstructure

To address challenges as noise sensitivity and low lateral resolution, Gersztenkorn and Marfurt (1999) develop a more robust method based on the energy ratio of eigenvalues of the covariance matrix to implement coherence calculation. Hereby, integrating adaptive spectral decomposition and coherence calculation, the amplitude spectrum at dominant frequency is taken as the input to construct the covariance matrix.

To suppress low-coherence artifacts, analytic trace and dip correction are adopted when constructing the covariance matrix. For certain 3D analysis cubes, each element C_{ij} of covariance matrix is computed as (Marfurt, 2006)

$$C_{ij}(t) = \sum_{k=-K}^K [a_i(t+k\Delta t - px_i - qy_i)a_j(t+k\Delta t - px_j - qy_j) + a_i^H(t+k\Delta t - px_i - qy_i)a_j^H(t+k\Delta t - px_j - qy_j)], \quad (3)$$

where a and a^H denote the dominant-frequency amplitude spectrum and the corresponding analytic trace. Assuming that the analysis point is at the center of the

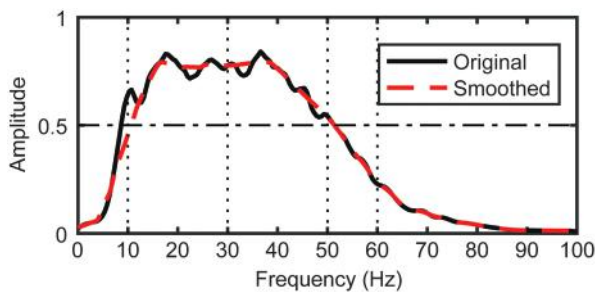


Figure 3. Statistic amplitude spectrum of input seismic data, where frequency 30 Hz is supposed to be the dominant frequency. According to the spectrum distribution, frequency 10, 30, and 60 Hz are picked to represent the low, medium, and high frequencies, respectively, and the corresponding amplitude spectra are extracted for coherence calculation.

analysis cube, its coordinate point is set as $(t, x = 0, y = 0)$. The terms i and j indicate the trace indexes in analysis cube, x_i and y_i (x_j and y_j) are the distances along the x - and y -axes of the i th (j th) trace, p and q are the apparent time dips of the analysis point, K denotes half of the time window sample, and Δt is the time-sampling increment.

The covariance matrix is a symmetric positive semi-definite matrix with all eigenvalues greater or equal to zero. Eigenstructure coherence is defined as a ratio of the dominant eigenvalue to the total energy within the analysis cube, expressed as (Gersztenkorn and Marfurt, 1999)

$$\text{Coh} = \frac{\lambda_1}{\text{Tr}(\mathbf{C})} = \frac{\lambda_1}{\sum_{j=1}^J c_{jj}} = \frac{\lambda_1}{\sum_{j=1}^J \lambda_j}, \quad (4)$$

where λ_1 is the largest eigenvalue of λ_j and $\text{Tr}(\mathbf{C})$ indicates the numerical trace of covariance matrix \mathbf{C} .

Super-resolution deep learning

Convolution filtering is a general-purpose technique used for a wide range of image processing tasks, some of which include sharpening, smoothing, and edge detection (Park and Schowengerdt, 1983; Sangwine and Ell, 2000). To enhance fault detection based on coherence, convolution filtering can be used to sharpen coherence images. In the context of image processing, a convolution is done by multiplying a pixel's and its surrounding pixels' color values within a window by a matrix, and the matrix is called a convolution filter, or a convolution kernel. The convolution process can be expressed as

$$v = d * k = \sum_{i=1}^q \sum_{j=1}^q d_{ij} k_{ij}, \quad (5)$$

where v is the output value of certain point, k_{ij} denotes the coefficient of a convolution kernel at position i, j , d_{ij} is the data value within convolution window corresponds to k_{ij} , q is the dimension of the kernel, assuming a square kernel. Normalization is usually performed to ensure the initial brightness or value range of input image or data is maintained. It should be noted that, without kernel flipping, the convolution operation performed here is actually a crosscorrelation, and it is conventionalized as convolution in image processing.

The size of a kernel is arbitrary, but 3×3 is often used, and differently sized kernels containing different patterns of numbers produce different results under convolution. Taking image sharpening as an example, a coherence image is set as input and three kernels with different weights are adopted. The sharpening results are shown in Figure 4. It demonstrates that the sharpening process accentuates edges and different kernels could give rise to various consequences. Meanwhile, there is a cost of adding noise during sharpening. Along

with increasing the extent of sharpening, more noise is introduced.

Based on the above discussion, convolution filtering depends on manual-set kernel weights and introduces side effects, such as adding noise. In contrast, CNN model is constructed automatically based on data-driven learning, whose optimal kernel weights are optimized. Thus, CNN-based deep learning is introduced to improve the quality of coherence images and therefore achieve fault detection enhancement.

Very deep SR (VDSR) (Kim et al., 2016) adopted in this paper is the first very deep model used in single-image SR, and examples demonstrated its significant improvement in SR accuracy and great potential in other image-restoration problems such as denoising and compression artifact removal. As shown in Figure 5, VDSR architecture is composed of 20-layer VGGNet (Simonyan and Zisserman, 2014). In VDSR, layers except the first and the last are of the same type: 64 convolution filter of the size 3×3 with rectified linear units (ReLUs) as the activation function. The first layer operates on the input image, and the last layer, used for image reconstruction, consists of a single filter of size 3×3 .

To train this deep neural network model, suitable data sets are used to provide features and labels of machine learning. For SR image reconstruction, features as LR images are prepared from HR images by down-sampling and interpolation and HR images are set as labels. Let vector \mathbf{X} denote an interpolated LR image and vector \mathbf{Y} an HR image. Given a training data set $\{\mathbf{X}_i, \mathbf{Y}_i\}$ with i from 1 to N , SR deep learning is to learn a model F nonlinearly mapping LR and HR images

$$\hat{\mathbf{Y}}_i = F(\mathbf{X}_i), \quad (6)$$

where $\hat{\mathbf{Y}}_i$ is an estimate of the target HR image \mathbf{Y}_i , N is the number of images for training, and F is expressed as a combination of multiple convolution kernels and ReLU functions.

Learning the end-to-end mapping function F requires the estimation of convolution kernel weights as network parameters. This is achieved through minimizing the loss between the reconstructed images and the corresponding ground truth HR images. The loss function mean square error (MSE) is expressed as

$$\text{MSE} = \frac{1}{N} \sum_{i=1}^N \|F(\mathbf{X}_i) - \mathbf{Y}_i\|^2. \quad (7)$$

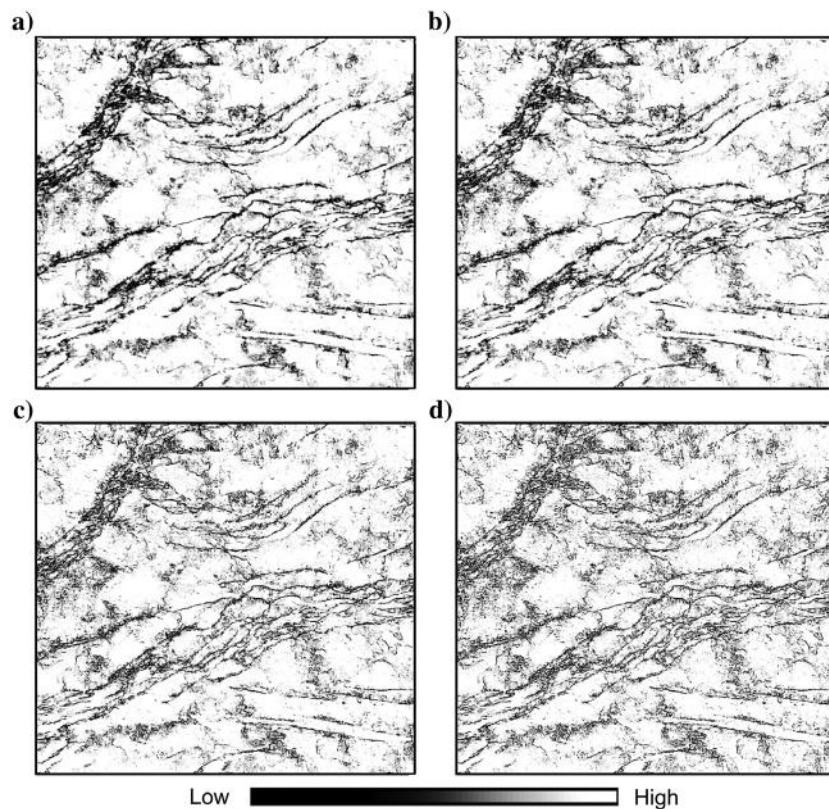


Figure 4. Coherence sharpening by convolutional filtering: (a) original coherence slice and (b-d) are sharpening results with different kernels.

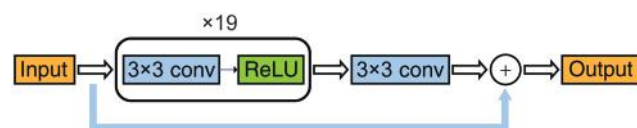


Figure 5. Sketch of the VDSR architecture, from Yang et al. (2018).

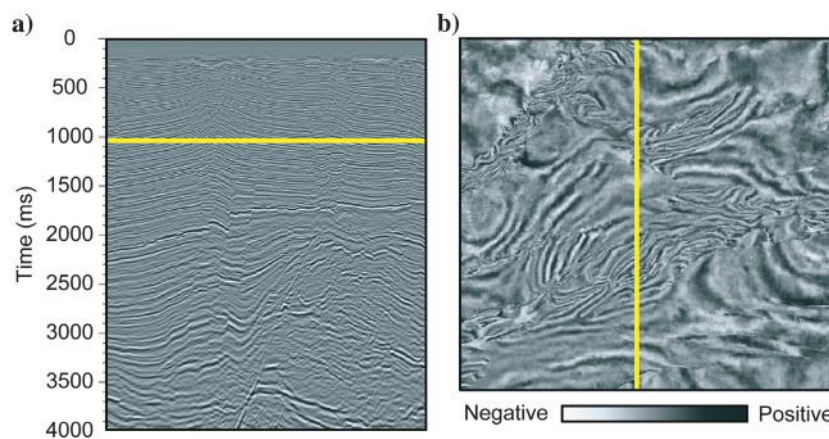


Figure 6. The 3D seismic data used for enhanced fault detection: (a) an inline section and (b) a time slice are extracted for demonstration, and the yellow lines denote the corresponding locations.

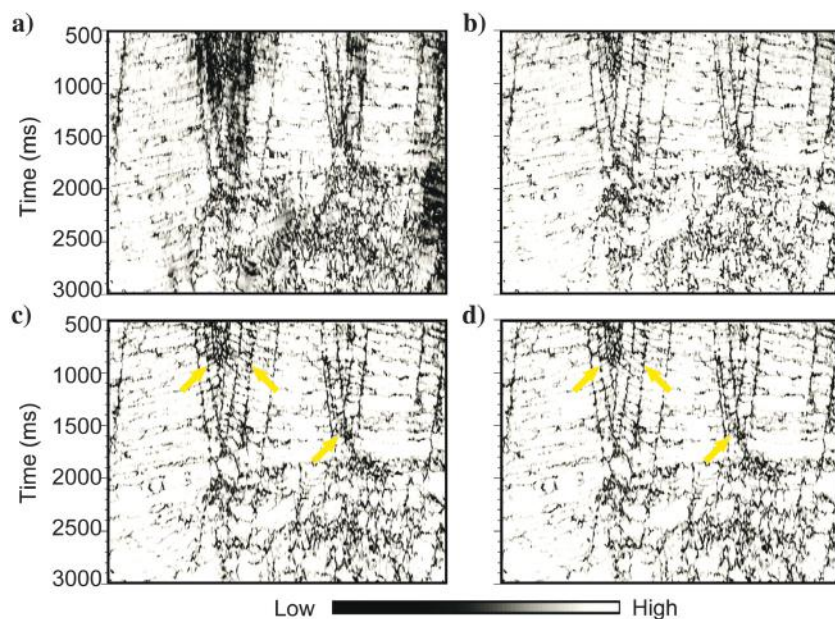


Figure 7. Fault detection of the inline section with dip correction and adaptive spectral decomposition: (a) coherence from seismic amplitude data without dip correction, (b) coherence from seismic amplitude data with dip correction, (c) coherence from adaptive frequency-optimized amplitude spectrum without dip correction, and (d) coherence from adaptive frequency-optimized amplitude spectrum with dip correction. The yellow arrows indicate some areas of improvements.

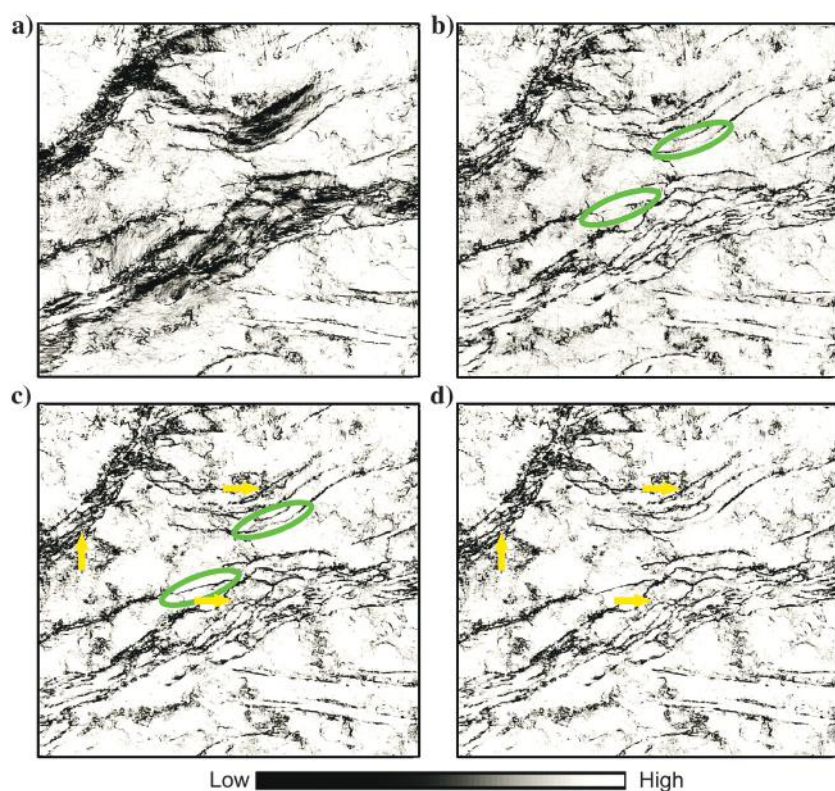


Figure 8. Fault detection of time slice with dip correction and adaptive spectral decomposition: (a) coherence from seismic amplitude data without dip correction, (b) coherence from seismic amplitude data with dip correction, (c) coherence from adaptive frequency-optimized amplitude spectrum without dip correction, and (d) coherence from adaptive frequency-optimized amplitude spectrum with dip correction. The green ellipses and yellow arrows indicate some areas of improvements.

To solve this optimization problem efficiently, Kim et al. (2016) use residual learning and a relatively big initial learning rate to accelerate convergence and use gradient clipping to prevent gradient explosion. More details of the optimization objectives for deep learning-based single-image SR can be found in Yang et al. (2018).

Different numerical metrics can then be used to evaluate the performance of SR model, when the ground truth images are available. For instance, peak signal-to-noise ratio (PSNR) is a widely used metric for quantitatively evaluating image restoration quality, and it is at least partially related to the perceptual quality. The PSNR (in dB) is defined as

$$\text{PSNR} = 10 \log_{10}(R^2/\text{MSE}), \quad (8)$$

where R is the maximum fluctuation in the input image data type. For example, if the input image has a double-precision floating-point data type, then R is 1. If it has an 8-bit unsigned integer data type, R is 255, etc. From equation 8, using MSE as the loss function favors a high PSNR.

From the above definition, VDSR is a type of CNN model originally used in SR image reconstruction and can also be extended to general image-processing tasks. Based on a specific fault-labeled data set, the VDSR CNN model can be optimized and used to enhance fault-detection performance.

Examples

To illustrate the performance of our new enhanced fault-detection method, some applications to a 3D survey acquired from Eastern China are presented. The study survey is located in a fault-depression basin, with a size of approximately 250 km². The study area has experienced multiple stages of fault tectonic movement, and faults are mainly distributed in the northeast-southwest direction (Zhang et al., 1996). The distribution of large faults and associated faults around them constituted oil-bearing structural traps. With high-fidelity denoising and reverse time migration, the migrated amplitude volume is of high resolution and high S/N.

An inline section and a time slice are extracted for demonstration, as shown in Figure 6. From the seismic amplitude

data, some faults can be observed with weak continuity and low resolution. Following the application of our proposed method, images of faults have been considerably enhanced.

Fault detection with adaptive spectral decomposition

Figure 7 shows fault-detection results of an inline section with dip correction and adaptive spectral decomposition. Comparing Figure 7a with Figure 7b, it is obvious that for seismic amplitude data, dip correction can dramatically improve the resolution and S/N of fault-detection results. Comparing Figure 7b and 7c, it can be concluded that coherence from an adaptive amplitude spectrum without dip correction is comparable to that from seismic amplitude data with dip correction in resolution and S/N at a certain degree, and even better in deep areas. Comparing Figure 7c and 7d, the improvement is not so distinct when incorporating dip correction to spectral-based fault detection, some S/N enhancements are pointed out with yellow arrows.

For the time slice, fault-detection results at 1024 ms are shown in Figure 8, where the influence of adaptive spectral decomposition and dip correction are taken into consideration. Same as Figure 7, dip correction can effectively improve resolution and S/N of coherence image calculated from seismic amplitude data. However, for that from adaptive amplitude spectrum, the improvement is not so obvious. Some differences are highlighted with yellow arrows in Figure 8c and 8d. In reviewing the literature, Sui et al. (2015) note that amplitude spectrum is not affected by the time delays in adjacent seismic traces caused by dipping structures. Their finding could partly corroborate the effect of dip correction on spectrum-based coherence. Additionally, comparing with the dip-corrected one (Figure 8b), coherence from adaptive amplitude spectrum (Figure 8c) provides high S/N and illuminates some certain scale of faults (shown in the green ellipses). Considering the importance of adaptive spectral decomposition and dip correction in fault detection, they are both adopted in the following examples.

Comparison of fault detections from adaptive amplitude spectrum and some specific-frequency amplitude spectra is presented in Figure 9. With varying depth, the coherence from the low-frequency spectrum highlights large and middle scale faults, respectively, and coherence from high-frequency spectrum shows more details of the fault distribution. To summarize, coherence of a specific-frequency

spectrum only picks out faults of a certain scale, while overlooking other information. In contrast, coherence from an adaptive dominant-frequency spectrum preferably characterizes fault systems of different scales at varying depths, exhibiting as a combination of multiple specific-frequency results.

Fault enhancement by SR deep learning

SR processing is incorporated to improve resolution and interpretability of fault-detection images. For fault-enhanced SR CNN model training, coherence images should be taken as input LR features, but it is almost impossible for us to prepare the corresponding HR label images. Taking advantage of transfer learning, 1000 fault-type or fracture-type images were collected to prepare the data set, then a VDSR CNN model is trained and transferred to coherence image SR processing. The reason why we collected these fault-type or fracture-type images is because of their similarity to fault-detection images. Some samples of the collected images are shown in Figure 10. During data-set preparation, collected images were taken as HR images and used to generate the corresponding LR images through down-

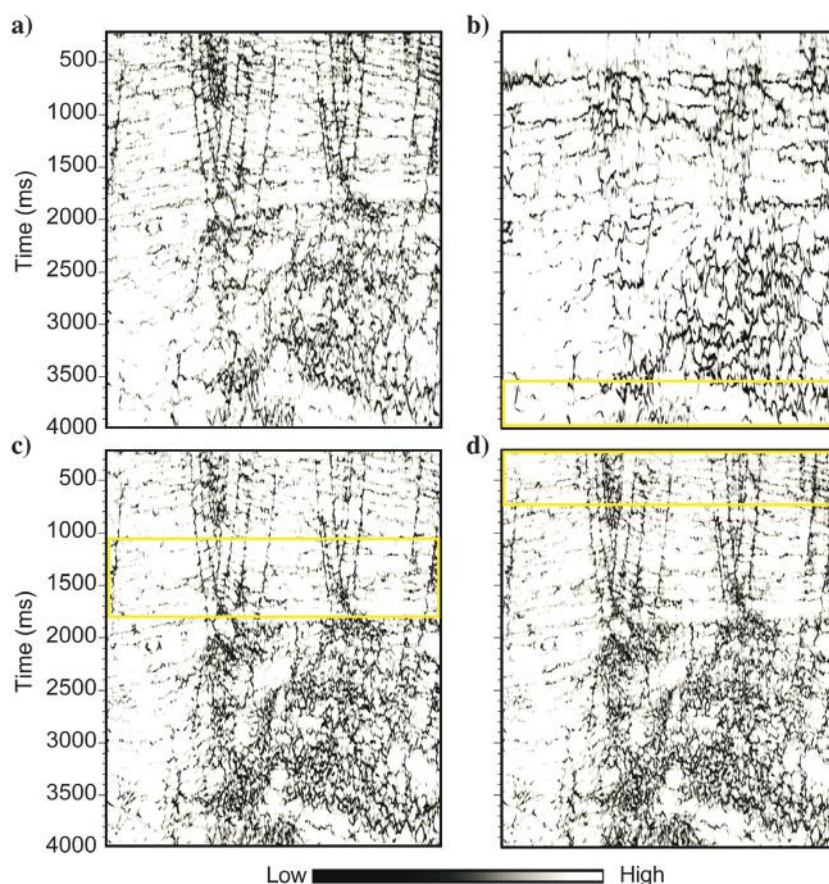


Figure 9. Comparison of fault-detection results from adaptive dominant-frequency spectrum and from the specific-frequency spectrum: (a) coherence from the adaptive dominant-frequency amplitude spectrum, (b) coherence from the 10 Hz frequency-amplitude spectrum, (c) coherence from the 30 Hz frequency-amplitude spectrum, and (d) coherence from the 60 Hz frequency-amplitude spectrum.

sampling and interpolation. HR images and LR images then composed the data set, as features and labels, respectively, for SR deep learning.

The implementation of SR deep learning was carried out in TensorFlow (Abadi et al., 2015), an open-source library from Google. An adaptive moment estimation optimizer (Kingma and Ba, 2014), an adaptive learning rate optimization algorithm, has been adopted to perform deep-learning optimization. Taking PSNR as a numerical metric, the training process is illustrated in Figure 11. The whole process involves 100,000 iteration steps, and the training and validation are showed. With the training iteration, the PSNR rapidly achieves a relatively high degree and then increases slowly in fluctuation. Inferring from the validation performance and its gap with the training PSNR, the trained SR CNN model is of good generalization and high accuracy.

For comparison, some SR image processing results of the B100 (Timofte et al., 2014) data set using VDSR model are presented here, shown in Figure 12. This shows that VDSR perfectly reconstructs sharp lines (Kim et al., 2016).

For fault SR enhancement, coherence images are input to a well-trained VDSR model to perform SR process-

ing. The enhanced results are shown in Figure 13, and two parts are magnified to explore details. From the magnified parts, it is obvious that after SR processing, the faults identified in coherence images are more contractive and the contrast ratio of the images is improved.

To get a more geologically promising fault-detection enhancement, we apply a VDSR CNN model to a specific fault-labeled data set with 200 samples. Five samples of the fault-labeled data set are shown in Figure 14.

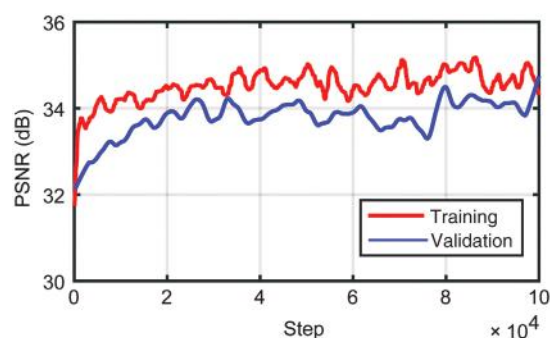


Figure 11. Training performance of VDSR model with an initial learning rate of 0.001.

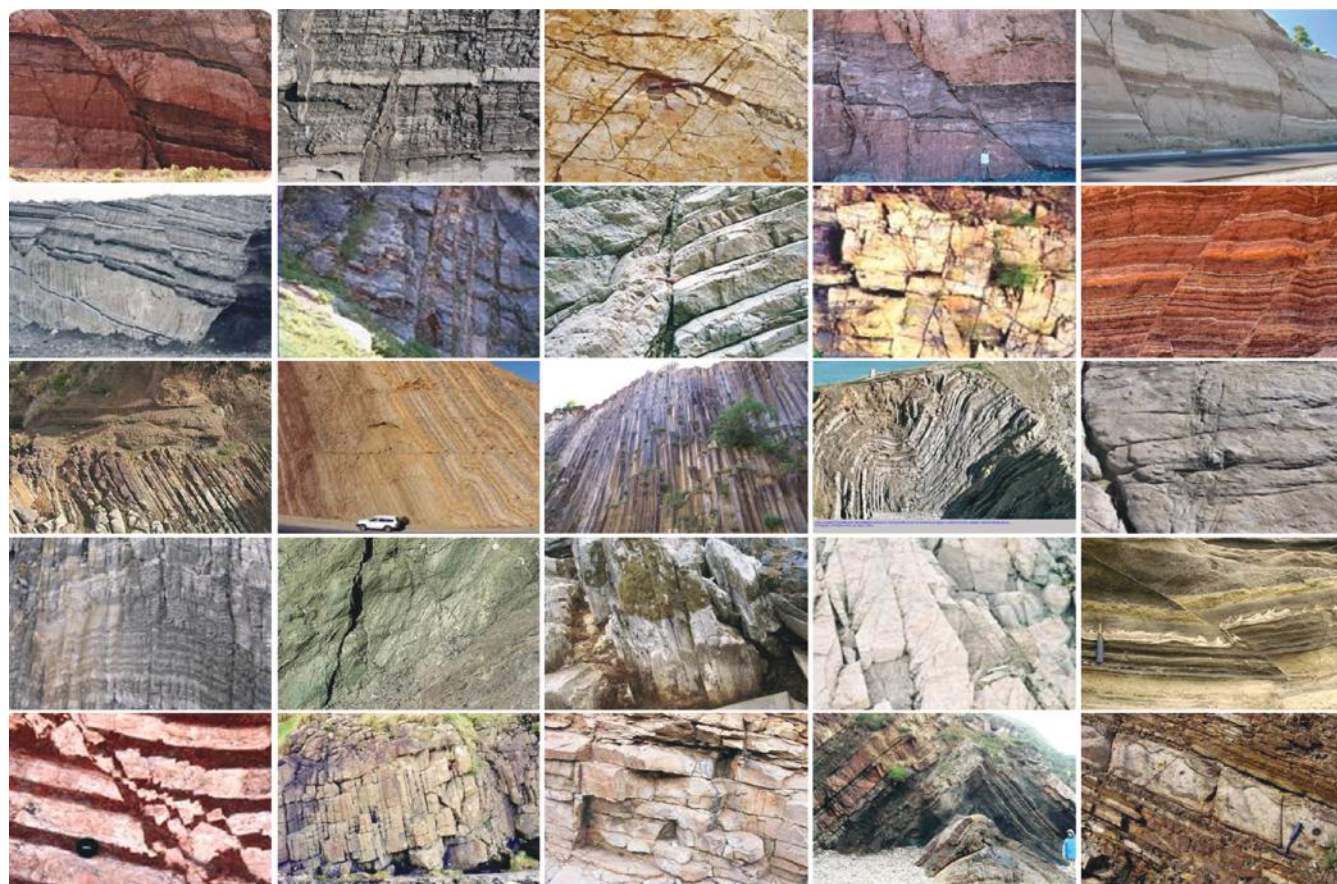


Figure 10. Some samples of fault-type or fracture-type images, courtesy of R. Luck, H. D. Maher Jr., B. Cardott, M. B. Miller, C. DeMets, J. Houghton, J. Toro, C. E. Jones, L. R. Alejano, J. Arzúa y María Veiga, T. Van Der Zaag, C. Bailey, Lagrima, I. West, C. Bentley, A. Alden, B. John, NASA, RWTH Aachen University, the Geological Survey of Northern Ireland, the University of Leeds, the University of Nebraska-Lincoln, the Geological Society of Australia Victoria, etc. These images were taken as HR feature images and used to generate the corresponding LR label images.

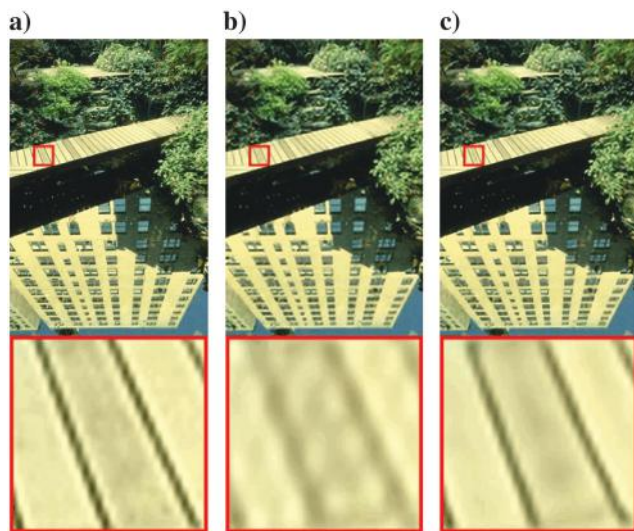


Figure 12. SR results of “148,026” (B100) from Kim et al. (2016): (a) ground truth image, (b) interpolated image as input, and (c) VDSR processed image.

Unlike the data set used in SR image processing, the input features are raw coherence images and target labels are fault-distribution images with faults manually interpreted from corresponding coherence images. During the preparation of this new data set, there is no need to perform downsampling or interpolation.

Based on the fault-labeled data set, VDSR CNN model is retrained. Taking the same coherence image used in Figure 13 as the input, the retrained CNN model outputs a better enhanced image. Figure 15 shows the input and corresponding enhanced coherence images. It is obvious that the resolution and S/N of the coherence image are effectively improved. Furthermore, the enhanced coherence image is more geologically interpretable, demonstrating more contractive fault distribution and more details of fault geometry. Focusing on the top-left part of the images, the mussy fault responses identified from original coherence image become much clearer after CNN fault-enhance processing. Major faults and their surrounding concomitant faults can be easily detected from the enhanced coherence image. Two parts are mag-

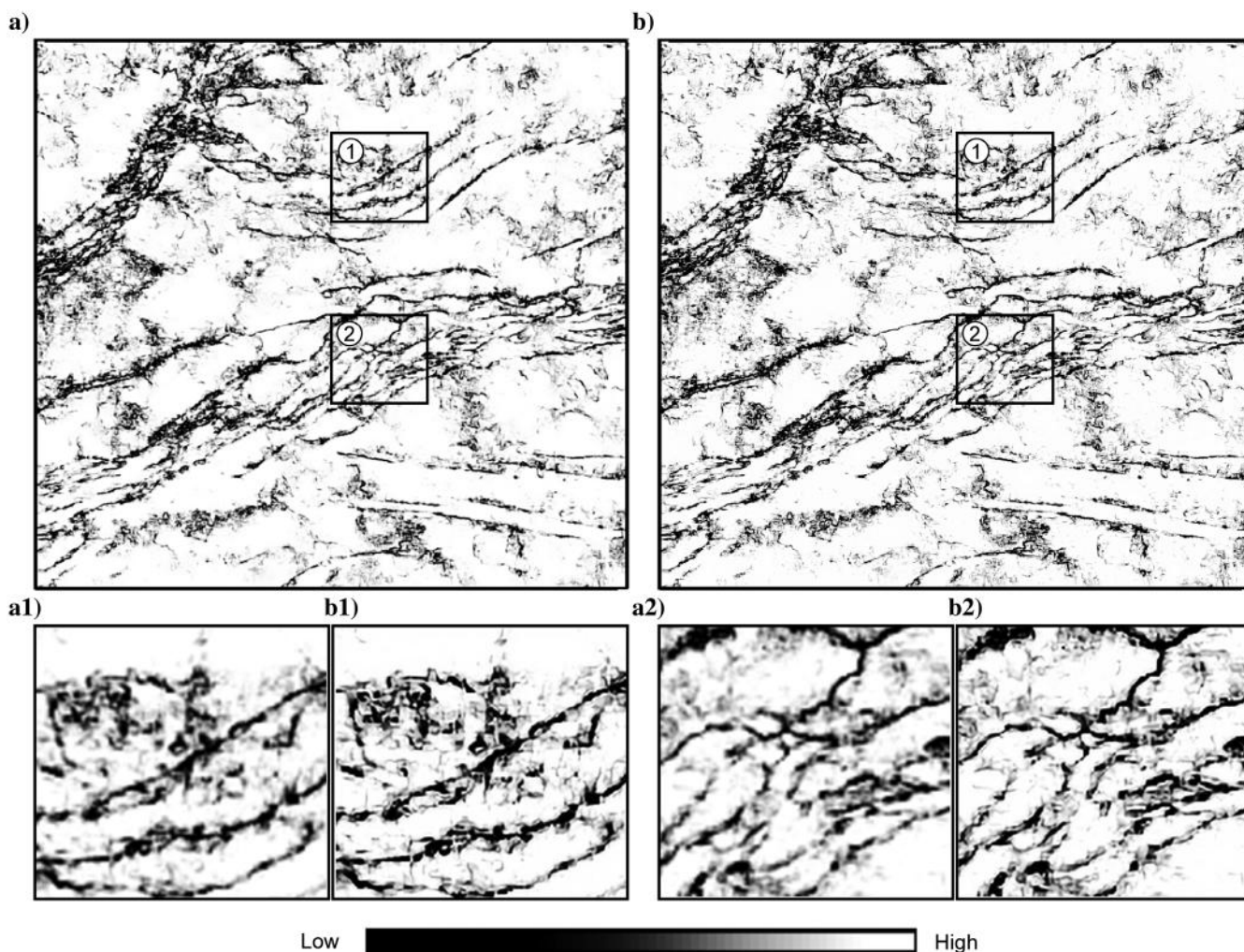


Figure 13. SR processing of the coherence image: (a) original image and (b) SR processed image. The dark rectangles partition some parts (labeled as ① and ②) to amplify the SR performance. The magnified parts and the corresponding SR processed results are shown in (a1), (a2) and (b1), (b2).

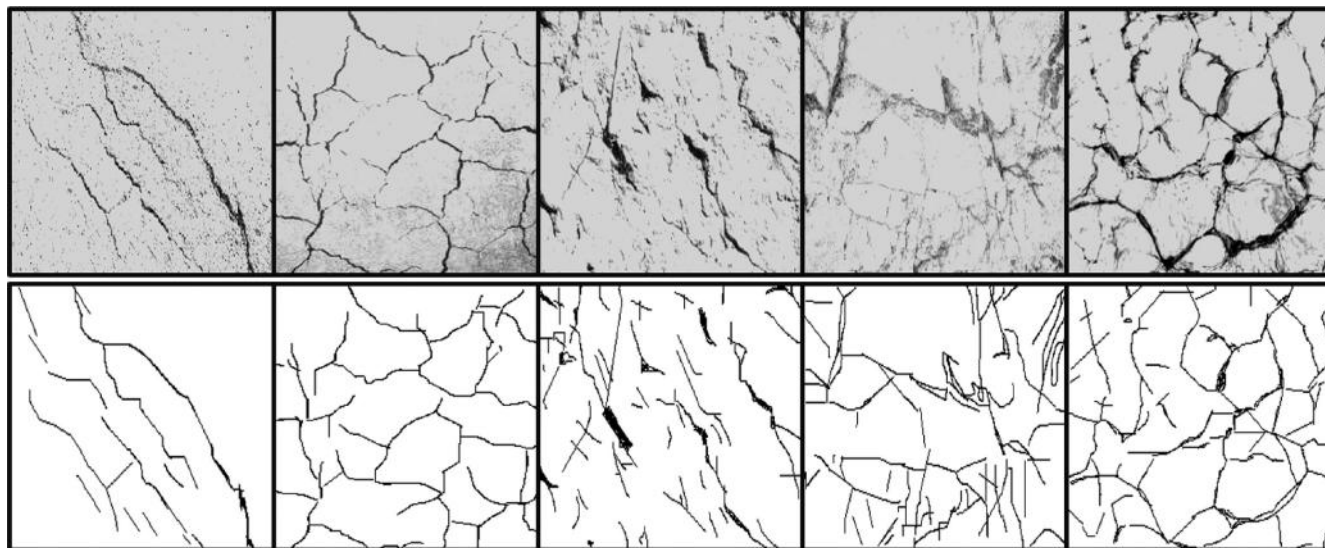


Figure 14. Some samples of the fault-labeled data set: The upper images are raw coherence images, and the lower images are the corresponding interpreted fault images.

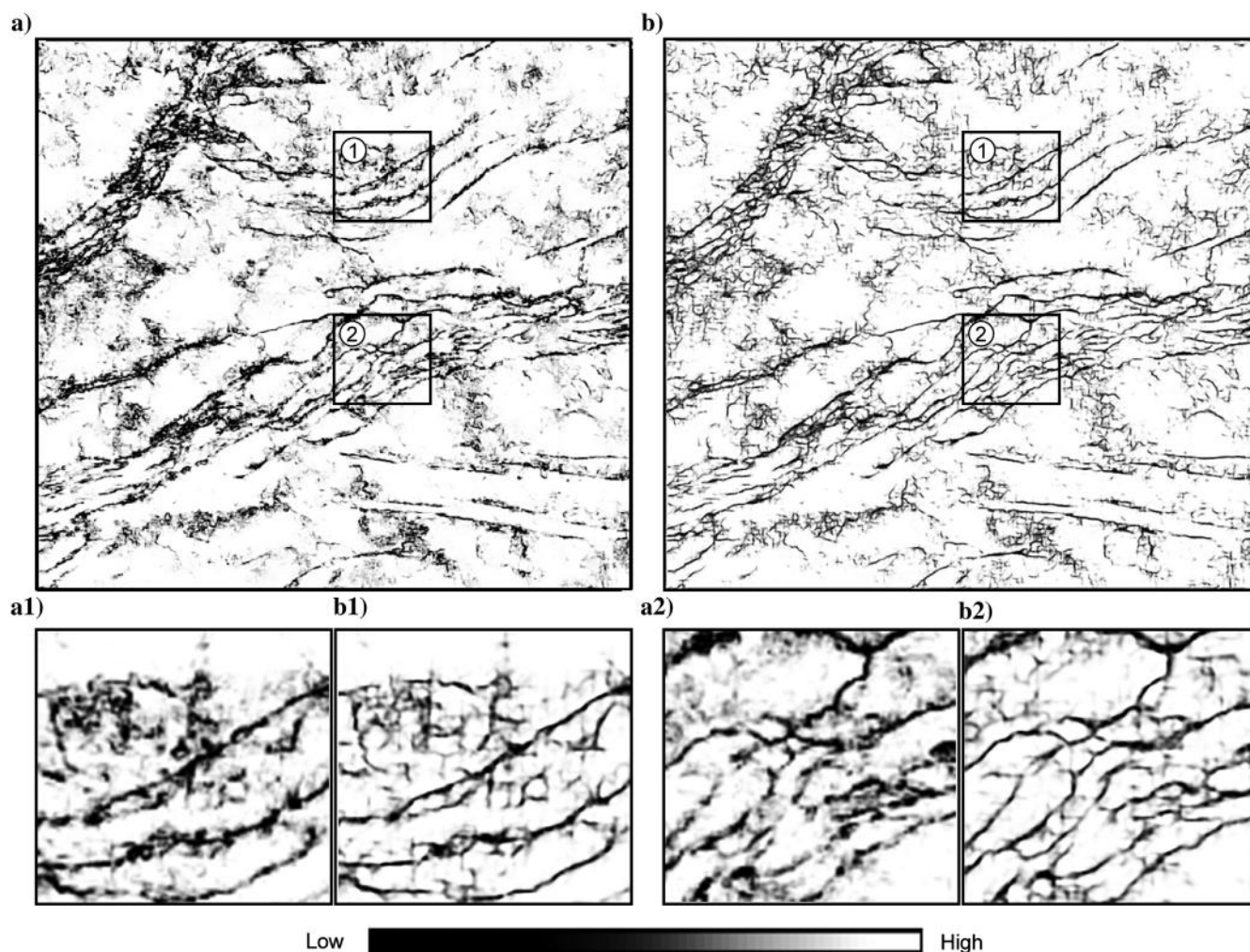


Figure 15. The CNN-based fault-enhancement processing of the coherence image: (a) original coherence image and (b) enhanced coherence image. The dark rectangles partition some parts (labeled as ① and ②) to show more details. The magnified original parts and the corresponding enhanced results are shown in (a1), (a2) and (b1), (b2).

nified to display more details of the enhanced performance. Despite the enhancements of resolution and S/N, the continuity of identified faults is also improved. From the above analysis, the enhancement performance of the proposed CNN deep-learning processing is geologically promising. Combining the results shown in Figure 13, it can be concluded that the performance of CNN deep learning depends on the selection of an appropriate data set.

Conclusion

Introducing adaptive spectral decomposition and SR deep learning into fault detection, we proposed a new method for enhanced fault detection, which adaptively identifies faults at different scales varying with depth (or time) with improved fault continuity, resolution, and S/N. The examples validated the effectiveness and advantage of this novel method. The incorporation of adaptive spectral decomposition provides comparable performance with dip correction on seismic amplitude data, eliminating tilted strata discontinuity artifacts, and highlighting certain scale of discontinuities that may be overprinted by other information. Furthermore, fault detection from adaptive dominant-frequency amplitude spectrum preferably characterizes fault systems of different scales at varying depths, exhibiting as a combination of multiple specific-frequency results. In other words, adaptive spectral decomposition fault detection has features of scale focus and multiple resolution. In addition, it accelerates fault-detection process without manually comparing various specific-frequency fault-detection results and reduces data storage concomitantly. Convolutional filtering sharpens the coherence images but with a side effect of adding noise, and the setting of appropriate kernels is a manual operation. Progressively, CNN-based SR deep learning optimizes the model parameters by data-driven learning and effectively improves the resolution of coherence images. Based on the fault-labeled data set, CNN deep learning further promotes the interpretability of coherence images with enhanced fault continuity, as well as improved resolution and S/N. Considering the generalization of a well-trained fault-enhance CNN model, it could be applied further to more fault-detection images for resolution and interpretability enhancement. In spite of the current processing of images, SR processing could be directly applied on digital data. In conclusion, the application of this new fault-detection method is an effective way to detect a different scale of faults with high resolution, and it helps interpreters quickly and clearly visualize complex subsurface fault systems. Inspiringly, the proposed enhanced techniques, including adaptive spectral decomposition, convolution filtering, and SR deep learning, can be regarded as some basic modules of fault detection or even other interpretation applications, and then assembled with other techniques to facilitate reservoir characterization.

Acknowledgments

This work was financially supported by the National Natural Science Foundation of China (grant no. 41674139) and the National Science and Technology Major Project (grant no. 2016ZX05033-02). The authors acknowledge the support and permission of PST Service Corporation to publish this paper. We also thank W. Tang at Intel for valuable discussions on the programming of CNN deep-learning implementation.

Data and materials availability

Data associated with this research are confidential and cannot be released.

References

- Abadi, M., A. Agarwal, P. Barham, E. Brevdo, Z. Chen, C. Citro, G. S. Corrado, A. Davis, J. Dean, M. Devin, S. Ghemawat, I. Goodfellow, A. Harp, G. Irving, M. Isard, Y. Jia, R. Jozefowicz, L. Kaiser, M. Kudlur, J. Levenberg, D. Mané, R. Monga, S. Moore, D. Murray, C. Olah, M. Schuster, J. Shlens, B. Steiner, I. Sutskever, K. Talwar, P. Tucker, V. Vanhoucke, V. Vasudevan, F. Viégas, O. Vinyals, P. Warden, M. Wattenberg, M. Wicke, Y. Yu, and X. Zheng, 2015, TensorFlow: Large-scale machine learning on heterogeneous systems, <https://www.tensorflow.org/about/bib>, accessed 5 June 2019.
- Alaei, B., 2012, Improved fault imaging by integration of frequency decomposition and fault attributes, example from Mid Norwegian Sea: 3rd International Conference on Fault and Top Seals, EAGE, doi: [10.3997/2214-4609.20143024](https://doi.org/10.3997/2214-4609.20143024).
- Alaei, B., and A. Torabi, 2017, Seismic imaging of fault damaged zone and its scaling relation with displacement: Interpretation, **5**, no. 4, SP83–SP93, doi: [10.1190/INT-2016-0230.1](https://doi.org/10.1190/INT-2016-0230.1).
- AlBinHassan, N. M., and K. Marfurt, 2003, Fault detection using Hough transforms: 73rd Annual International Meeting, SEG, Expanded Abstracts, 1719–1721, doi: [10.1190/1.1817639](https://doi.org/10.1190/1.1817639).
- Al-Dossary, S., and K. J. Marfurt, 2007, Lineament-preserving filtering: Geophysics, **72**, no. 1, P1–P8, doi: [10.1190/1.2387138](https://doi.org/10.1190/1.2387138).
- Bahorich, M., and S. Farmer, 1995, 3-D seismic discontinuity for faults and stratigraphic features: The coherence cube: The Leading Edge, **14**, 1053–1058, doi: [10.1190/1.1437077](https://doi.org/10.1190/1.1437077).
- Bakker, P., 2002, Image structure analysis for seismic interpretation: Ph.D. thesis, Delft University of Technology.
- Barnes, A. E., 2006, A filter to improve seismic discontinuity data for fault interpretation: Geophysics, **71**, no. 3, P1–P4, doi: [10.1190/1.2195988](https://doi.org/10.1190/1.2195988).
- Chopra, S., 2002, Coherence cube and beyond: First Break, **20**, 27–33.
- Chopra, S., and K. J. Marfurt, 2016, Spectral decomposition and spectral balancing of seismic data: The Leading Edge, **35**, 176–179, doi: [10.1190/le35020176.1](https://doi.org/10.1190/le35020176.1).

- Chopra, S., and K. J. Marfurt, 2017, Volumetric fault image enhancement: Some applications: *Interpretation*, **5**, no. 2, T151–T161, doi: [10.1190/int-2016-0129.1](https://doi.org/10.1190/int-2016-0129.1).
- Chopra, S., V. Sudhakar, G. Larsen, and H. Leong, 2000, Azimuth-based coherence for detecting faults and fractures: *World Oil*, **221**, 57–64.
- Cohen, I., N. Coult, and A. A. Vassiliou, 2006, Detection and extraction of fault surfaces in 3D seismic data: *Geophysics*, **71**, no. 4, P21–P27, doi: [10.1190/1.2215357](https://doi.org/10.1190/1.2215357).
- Di, H., M. Shafiq, and G. AlRegib, 2018, Patch-level MLP classification for improved fault detection: 88th Annual International Meeting, SEG, Expanded Abstracts, 2211–2215, doi: [10.1190/segam2018-2996921.1](https://doi.org/10.1190/segam2018-2996921.1).
- Dong, C., C. C. Loy, K. He, and X. Tang, 2016, Image super-resolution using deep convolutional networks: *IEEE Transactions on Pattern Analysis and Machine Intelligence*, **38**, 295–307.
- Fehmers, G. C., and C. F. Höcker, 2003, Fast structural interpretation with structure-oriented filtering: *Geophysics*, **68**, 1286–1293, doi: [10.1190/1.1598121](https://doi.org/10.1190/1.1598121).
- Gersztenkorn, A., and K. J. Marfurt, 1999, Eigenstructure-based coherence computations as an aid to 3-D structural and stratigraphic mapping: *Geophysics*, **64**, 1468–1479, doi: [10.1190/1.1444651](https://doi.org/10.1190/1.1444651).
- Gersztenkorn, A., J. Sharp, and K. Marfurt, 1999, Delineation of tectonic features offshore Trinidad using 3-D seismic coherence: *The Leading Edge*, **18**, 1000–1008, doi: [10.1190/1.1438422](https://doi.org/10.1190/1.1438422).
- Guo, B., L. Li, and Y. Luo, 2018a, A new method for automatic seismic fault detection using convolutional neural network: 88th Annual International Meeting, SEG, Expanded Abstracts, 1951–1955, doi: [10.1190/segam2018-2995894.1](https://doi.org/10.1190/segam2018-2995894.1).
- Guo, J., J. G. Rubino, N. D. Barbosa, S. Glubokovskikh, and B. Gurevich, 2018b, Seismic dispersion and attenuation in saturated porous rocks with aligned fractures of finite thickness: Theory and numerical simulations. Part 1: P-wave perpendicular to the fracture plane: *Geophysics*, **83**, no. 1, WA49–WA62, doi: [10.1190/geo2017-0065.1](https://doi.org/10.1190/geo2017-0065.1).
- Guo, J., J. G. Rubino, N. D. Barbosa, S. Glubokovskikh, and B. Gurevich, 2018c, Seismic dispersion and attenuation in saturated porous rocks with aligned fractures of finite thickness: Theory and numerical simulations. Part II: Frequency-dependent anisotropy: *Geophysics*, **83**, no. 1, WA63–WA71, doi: [10.1190/geo2017-0066.1](https://doi.org/10.1190/geo2017-0066.1).
- Hale, D., 2009, Structure-oriented smoothing and semblance: Colorado School of Mines, CWP Report 635.
- Hale, D., 2013, Methods to compute fault images, extract fault surfaces, and estimate fault throws from 3D seismic images: *Geophysics*, **78**, no. 2, O33–O43, doi: [10.1190/geo2012-0331.1](https://doi.org/10.1190/geo2012-0331.1).
- Höcker, C. F., and G. C. Fehmers, 2002, Fast structural interpretation with structure-oriented filtering: *The Leading Edge*, **21**, 238–243, doi: [10.1190/1.1463775](https://doi.org/10.1190/1.1463775).
- Honório, B. C. Z., U. M. d. C. Correia, M. C. d. Matos, and A. C. Vidal, 2017, Similarity attributes from differential resolution components: *Interpretation*, **5**, no. 1, T65–T73, doi: [10.1190/int-2015-0211.1](https://doi.org/10.1190/int-2015-0211.1).
- Huang, L., X. Dong, and T. E. Clee, 2017, A scalable deep learning platform for identifying geologic features from seismic attributes: *The Leading Edge*, **36**, 249–256, doi: [10.1190/tle36030249.1](https://doi.org/10.1190/tle36030249.1).
- Kim, J., J. Kwon Lee, and K. Mu Lee, 2016, Accurate image super-resolution using very deep convolutional networks: *Proceedings of the IEEE Conference on Computer Vision and Pattern Recognition*, 1646–1654.
- Kingma, D. P., and J. Ba, 2014, Adam: A method for stochastic optimization: *arXiv preprint arXiv:1412.6980*.
- LeCun, Y., Y. Bengio, and G. Hinton, 2015, Deep learning: *Nature*, **521**, 436–444, doi: [10.1038/nature14539](https://doi.org/10.1038/nature14539).
- LeCun, Y., B. E. Boser, J. S. Denker, D. Henderson, R. E. Howard, W. E. Hubbard, and L. D. Jackel, 1990, Handwritten digit recognition with a back-propagation network: *Advances in Neural Information Processing Systems*, 396–404.
- Li, F., and W. Lu, 2014, Coherence attribute at different spectral scales: *Interpretation*, **2**, no. 1, SA99–SA106.
- Li, F., J. Qi, B. Lyu, and K. J. Marfurt, 2018, Multispectral coherence: *Interpretation*, **6**, no. 1, T61–T69, doi: [10.1190/int-2017-0112.1](https://doi.org/10.1190/int-2017-0112.1).
- Luo, Y., M. Marhoon, S. Al-Dossary, and M. Alfaraj, 2002, Edge-preserving smoothing and applications: *The Leading Edge*, **21**, 136–158, doi: [10.1190/1.1452603](https://doi.org/10.1190/1.1452603).
- Machado, G., A. Alali, B. Hutchinson, O. Olorunsola, and K. J. Marfurt, 2016, Display and enhancement of volumetric fault images: *Interpretation*, **4**, no. 1, SB51–SB61, doi: [10.1190/INT-2015-0104.1](https://doi.org/10.1190/INT-2015-0104.1).
- Marfurt, K., 2017, Interpretational aspects of multispectral coherence: 79th Annual International Conference and Exhibition, EAGE, Extended Abstracts, doi: [10.3997/2214-4609.201700528](https://doi.org/10.3997/2214-4609.201700528).
- Marfurt, K. J., 2006, Robust estimates of 3D reflector dip and azimuth: *Geophysics*, **71**, no. 4, P29–P40, doi: [10.1190/1.2213049](https://doi.org/10.1190/1.2213049).
- Marfurt, K. J., R. L. Kirlin, S. L. Farmer, and M. S. Bahorich, 1998, 3-D seismic attributes using a semblance-based coherency algorithm: *Geophysics*, **63**, 1150–1165, doi: [10.1190/1.1444415](https://doi.org/10.1190/1.1444415).
- Marfurt, K. J., V. Sudhakar, A. Gersztenkorn, K. D. Crawford, and S. E. Nissen, 1999, Coherency calculations in the presence of structural dip: *Geophysics*, **64**, 104–111, doi: [10.1190/1.1444508](https://doi.org/10.1190/1.1444508).
- Park, S. K., and R. A. Schowengerdt, 1983, Image reconstruction by parametric cubic convolution: *Computer Vision, Graphics, and Image Processing*, **23**, 258–272, doi: [10.1016/0734-189X\(83\)90026-9](https://doi.org/10.1016/0734-189X(83)90026-9).
- Pedersen, S. I., T. Randen, L. Sonneland, and Ø. Steen, 2002, Automatic fault extraction using artificial ants: 72nd Annual International Meeting, SEG, Expanded Abstracts, 512–515, doi: [10.1190/1.1817297](https://doi.org/10.1190/1.1817297).
- Pedersen, S. I., T. Skov, A. Hetlelid, P. Fayemendy, T. Randen, and L. Sonneland, 2003, New paradigm of fault interpretation: 73rd Annual International Meeting,

- SEG, Expanded Abstracts, 350–353, doi: [10.1190/1.1817918](https://doi.org/10.1190/1.1817918).
- Pham, N., S. Fomel, and D. Dunlap, 2018, Automatic channel detection using deep learning: 88th Annual International Meeting, SEG, Expanded Abstracts, 2026–2030, doi: [10.1190/segam2018-2991756.1](https://doi.org/10.1190/segam2018-2991756.1).
- Pinnegar, C. R., and L. Mansinha, 2003, The S-transform with windows of arbitrary and varying shape: *Geophysics*, **68**, 381–385, doi: [10.1190/1.1543223](https://doi.org/10.1190/1.1543223).
- Qi, J., G. Machado, and K. Marfurt, 2017, A workflow to skeletonize faults and stratigraphic features: *Geophysics*, **82**, no. 4, O57–O70, doi: [10.1190/geo2016-0641.1](https://doi.org/10.1190/geo2016-0641.1).
- Sangwine, S. J., and T. A. Ell, 2000, Color image filters based on hypercomplex convolution: *IEEE Proceedings-Vision, Image and Signal Processing*, **147**, 89–93.
- Shi, Y., X. Wu, and S. Fomel, 2018, Automatic salt-body classification using a deep convolutional neural network: 88th Annual International Meeting, SEG, Expanded Abstracts, 1971–1975, doi: [10.1190/segam2018-2997304.1](https://doi.org/10.1190/segam2018-2997304.1).
- Simonyan, K., and A. Zisserman, 2014, Very deep convolutional networks for large-scale image recognition: *arXiv preprint arXiv:1409.1556*.
- Stockwell, R., L. Mansinha, and R. Lowe, 1996, Localization of the complex spectrum: The S transform: *IEEE Transactions on Signal Processing*, **44**, 998–1001.
- Sui, J., X. Zheng, and Y. Li, 2015, A seismic coherency method using spectral amplitudes: *Applied Geophysics*, **12**, 353–361, doi: [10.1007/s11770-015-0501-5](https://doi.org/10.1007/s11770-015-0501-5).
- Timofte, R., V. De Smet, and L. Van Gool, 2014, A+: Adjusted anchored neighborhood regression for fast super-resolution: *Asian Conference on Computer Vision*, 111–126.
- Wang, X., J. Gao, W. Chen, C. Yang, and Z. Zhu, 2016, Detecting method of seismic discontinuities based on high dimensional continuous wavelet transform: *Chinese Journal of Geophysics-Chinese Edition*, **59**, 3394–3407.
- Wang, X., M. Su, J. Liu, W. Zhu, J. Zhao, D. Wang, C. Liu, and Y. Tang, 2002, Computation of seismic coherence cube based on wavelet transform and its application: *Geophysical Prospecting for Petroleum*, **41**, 334–338.
- Wu, W.-R., and A. Kundu, 1991, A new type of modified trimmed mean filter: *Electronic Imaging '91, SPIE*, 13–23.
- Wu, X., 2017, Directional structure-tensor-based coherence to detect seismic faults and channels: *Geophysics*, **82**, no. 2, A13–A17, doi: [10.1190/geo2016-0473.1](https://doi.org/10.1190/geo2016-0473.1).
- Wu, X., and S. Fomel, 2018, Automatic fault interpretation with optimal surface voting: *Geophysics*, **83**, no. 5, O67–O82, doi: [10.1190/geo2018-0115.1](https://doi.org/10.1190/geo2018-0115.1).
- Wu, X., and Z. Guo, 2019, Detecting faults and channels while enhancing seismic structural and stratigraphic features: *Interpretation*, **7**, no. 1, T155–T166, doi: [10.1190/INT-2017-0174.1](https://doi.org/10.1190/INT-2017-0174.1).
- Wu, X., and D. Hale, 2016, 3D seismic image processing for faults: *Geophysics*, **81**, no. 2, IM1–IM11, doi: [10.1190/geo2015-0380.1](https://doi.org/10.1190/geo2015-0380.1).
- Wu, X., L. Liang, Y. Shi, and S. Fomel, 2019, FaultSeg3D: Using synthetic datasets to train an end-to-end convolutional neural network for 3D seismic fault segmentation: *Geophysics*, **84**, no. 3, IM35–IM45, doi: [10.1190/geo2018-0646.1](https://doi.org/10.1190/geo2018-0646.1).
- Wu, X., Y. Shi, S. Fomel, and L. Liang, 2018, Convolutional neural networks for fault interpretation in seismic images: 88th Annual International Meeting, SEG, Expanded Abstracts, 1946–1950, doi: [10.1190/segam2018-2995341.1](https://doi.org/10.1190/segam2018-2995341.1).
- Wu, X., and Z. Zhu, 2017, Methods to enhance seismic faults and construct fault surfaces: *Computers and Geosciences*, **107**, 37–48.
- Yang, W., X. Zhang, Y. Tian, W. Wang, and J.-H. Xue, 2018, Deep learning for single image super-resolution: A brief review: *arXiv preprint arXiv:1808.03344*.
- Yuan, Z., J. Tang, Y. Shan, L. Deng, J. Wei, and C. Li, 2015, A discontinuity detection strategy based on spectral decomposition: 77th Annual International Conference and Exhibition, EAGE, Extended Abstracts, doi: [10.3997/2214-4609.201413122](https://doi.org/10.3997/2214-4609.201413122).
- Zhang, S., S. Tian, S. Zhu, Q. Zhang, and H. Zhou, 1996, Fracture structure and hydrocarbon third migration in Nanpu depression: *Oil and Gas Geology*, **17**, 262–267.
- Zhao, T., and P. Mukhopadhyay, 2018, A fault-detection workflow using deep learning and image processing: 88th Annual International Meeting, SEG, Expanded Abstracts, 1966–1970, doi: [10.1190/segam2018-2997005.1](https://doi.org/10.1190/segam2018-2997005.1).

Biographies and photographs of the authors are not available.